5B.1 THE T-REX VALLEY WIND INTERCOMPARISON PROJECT

Juerg Schmidli*, B.J. Billings, R. Burton, F.K. Chow, S.F.J. De Wekker, J.D. Doyle, V. Grubisic, T.R. Holt, Q. Jiang, K.A. Lundquist, A.N. Ross, P. Sheridan, S. Vosper, C.D. Whiteman, A.A. Wyszogrodzki, G. Zaengl, S. Zhong

*NCAR, Boulder, Colorado

1 INTRODUCTION

An accurate simulation of the evolution of the atmospheric boundary layer is very important, as the evolution of the boundary layer sets the stage for many weather phenomena, such as deep convection. Over mountain areas the evolution of the boundary layer is particularly complex, due to the nonlinear interaction between boundary layer turbulence and thermally-induced mesoscale wind systems, such as the slope and valley winds. As the horizontal resolution of operational forecasts progresses to finer and finer resolution, more and more of the thermally-induced mesoscale wind systems can be explicitly resolved, and it is very timely to document the current state-of-the-art of mesoscale models at simulating the coupled evolution of the mountain boundary layer and the valley wind system.

In this paper we present an intercomparison of valley wind simulations for an idealized valley-plain configuration using eight state-of-the-art mesoscale models with a grid spacing of 1 km. Different sets of three-dimensional simulations are used to explore the effects of varying model dynamical cores and physical parameterizations. This intercomparison project was conducted as part of the Terrain-induced Rotor Experiment (T-REX; Grubisic et al., 2008).

2 EXPERIMENTAL DESIGN

Two sets of simulations were carried out in order to explore the relative role of the model dynamical cores, turbulence mixing parameterizations, radiation transfer and land surface schemes. A set of "uncoupled" simulations used a prescribed surface heat flux, and a set of "coupled" simulations used comprehensive model physics (radiation transfer scheme and land surface model). Although the setup for both sets of simulations is described below, this paper will focus on the results from the coupled simulations.

2.1 General setup

The intercomparison is based on the idealized valley-plain system shown in Fig. 1. This setup is similar to configurations used in previous studies (Li and Atkinson, 1999; Rampanelli et al., 2004). The topography was chosen to satisfy the criteria listed in Rampanelli et al. (2004): (1) A horizontal valley floor, so that the along-valley wind has no upslope contribution, (2) a long valley, so that the along-valley flow can develop unhindered from numerical boundary conditions in the along-valley direction, (3) moderately steep valley slopes which can be adequately represented by current mesoscale models. In contrast to previous studies, a large computational domain and periodic lateral boundary conditions were chosen in order to minimize the influence of the lateral boundaries on the simulated flow.

The analytical expression for the topography used is given by

$$z = h(x,y) = h_p h_x(x) h_y(y) \tag{1}$$

where

$$h_x(x) = \begin{cases} 0 & |x| \le V_x \\ \frac{1}{2} - \frac{1}{2}\cos\left(\pi \frac{|x|-V_x}{S_x}\right) & V_x < |x| < X_2 \\ 1 & X_2 \le |x| \le X_3 \\ \frac{1}{2} + \frac{1}{2}\cos\left(\pi \frac{|x|-X_3}{S_x}\right) & X_3 < |x| < X_4 \\ 0 & |x| \ge X_4 \end{cases} \tag{2}$$

and

$$h_y(y) = \begin{cases} 1 & |y| \le P_y \\ \frac{1}{2} + \frac{1}{2}\cos\left(\pi \frac{|y|-P_y}{S_y}\right) & P_y < |y| < Y_2 \\ 0 & |y| \ge Y_2, \end{cases} \tag{3}$$

with valley depth $h_p = 1.5\,\text{km}$, $V_x = 0.5\,\text{km}$ (valley floor half width), $S_x = 9\,\text{km}$ (sloping sidewall width), $P_x = 1\,\text{km}$ (plateau width in cross-valley direction), $P_y = 100\,\text{km}$ (plateau half width in along-valley direction), $S_y = 9\,\text{km}$, and $X_2 = V_x + S_x$, $X_3 = V_x + S_x + P_x$, $X_4 = V_x + 2S_x + P_x$, $Y_2 = P_y + S_y$.

The simulations are started from an atmosphere at rest. The initial condition for the atmosphere is given by the potential temperature distribution

$$\theta(z) = \theta_s + \Gamma z + \Delta\theta[1 - \exp(-\beta z)] \tag{4}$$

where $\theta_s = 280\,\text{K}$, $\Gamma = 3.2\,\text{K km}^{-1}$, $\Delta\theta = 5\,\text{K}$, and $\beta = 0.002\,\text{m}^{-1}$, the surface pressure $p_s = 1000\,\text{hPa}$, and a constant relative humidity of 40%. The initial

temperature profile describes an atmosphere with a constant stratification of $N \approx 0.011\,\mathrm{s}^{-1}$ with a superimposed near-surface stable layer.

The computational domain of the simulations is 400 km in the y (along valley) direction and 120 km in the x (across valley) direction. The grid spacing is 1 km in both directions. In the vertical, the computational domain extends to at least 6.2 km and the grid spacing varies from 20 m near the ground to a maximum of 200 m above 2 km. The lateral boundary conditions are periodic, unless that option was not available for a particular model. As top boundary conditions a Rayleigh sponge was specified. All simulations are run with the Coriolis force turned off.

The models were integrated for 12 hours from sunrise (0600 local time (LT)) to sunset (1800 LT).

2.2 Uncoupled simulations

For the uncoupled simulations the surface sensible heat flux is given by

$$Q(t) = Q_0 \sin(\omega t) \tag{5}$$

where $Q_0 = 200\,\mathrm{W\,m}^{-2}$, $\omega = 2\pi/24\,\mathrm{h}^{-1}$, and the time t denotes hours since sunrise. The uncoupled simulations use free slip lower boundary conditions (i.e. zero momentum and latent heat flux).

2.3 Coupled simulations

In the coupled simulations the surface sensible heat flux is determined by the model physics, that is by the coupled land surface-atmosphere system. Additional specifications include

- Radiative forcing determined by the location (36° N, 0° E) and time of year 21 March 2007.
- Uniform land surface characteristics: soil type is sandy loam; vegetation is semidesert with LAI 1.5, vegetation fraction 0.1, roughness length 0.1 m. Albedo is set to 0.27, if it is not determined implicitly by the land surface model.
- Soil initialization: soil temperature is set equal to atmospheric surface temperature, soil moisture saturation ratio is 20 %.

2.4 Valley wind theory

Why does the above setup produce a valley wind? It is well known, that thermally-induced valley winds are generated by locally developed along-valley pressure gradients produced hydrostatically from temperature differences along the valley's axis and between the valley and the adjacent plains (Whiteman, 2000). The along-valley and valley-plain temperature differences can be produced by at least two factors: differences in the surface sensible heat flux, and by the valley volume effect (Wagner, 1938; Steinacker, 1984). The first factor is excluded for the uncoupled simulations, but both factors may be important for the coupled simulations.

2.5 Models

Table 1 gives a brief description of some of the main characteristics of the eight mesoscale models. Note that while most models use a non-local PBL-type turbulence scheme, i.e. nonlocal diffusion, mass flux scheme, or a TKE-based scheme with a nonlocal turbulent length scale, EULAG and WRF-TKE use a local TKE closure. All models, except RAMS, use periodic lateral boundary conditions. RAMS employs open lateral boundary conditions.

2.6 Intercomparison procedure

To make the results easily comparable, all variables from each of the models were interpolated to a destaggered grid in a common NetCDF file format.

3 RESULTS

In this section the results for the coupled simulations are presented. It should be noted that the RAMS results are not directly comparable to the other models, especially after 1200 LT. There is significant flow (larger $0.5\,\mathrm{m\,s}^{-1}$) through the lateral boundaries by 1130 LT which increases to over $2\,\mathrm{m\,s}^{-1}$ in the afternoon. No results will be presented for EULAG and UM, as there are still some questions regarding the model runs.

3.1 Forcing and mean temperature response

Figure 2 compares time evolution of the surface sensible heat flux and the resulting potential temperature evolution for a valley cross section located 20 km upvalley from the valley entrance, to the corresponding evolution over the plains. The differences between the models in timing and magnitude of the sensible heat flux is reflected in the corresponding evolution of the vertically-averaged potential temperature. The area-averaged surface sensible heat flux in the valley is consistently larger than the corresponding heat flux over the plains. The maximum surface sensible heat flux over the plain is only 67 % to 88 % of the corresponding valley value. It can be expected that this valley-plain difference in surface sensible heat flux will contribute to the strength of the valley wind, in addition to the valley volume effect, and to some of the differences between the models.

Table 1: Model Description. The following abbreviations are used: h for horizontal, v for vertical, c for computational mixing, SISL for semi-implicit semi-Lagrangian, NLD for nonlocal diffusion, MF for mass flux, D for Deardorff-based TKE scheme, MY for Mellor-Yamada based TKE scheme, NL for non-local turbulent length scale, and SLI for incoming radiation as a function of slope inclination.

Model	Time Differencing	dt [s]	Spatial Differencing	Turbulence Mixing Scheme	Horizontal Mixing	SLI
ARPS	Leapfrog 2nd ord	12	h: 4th ord v: 2nd ord	1.5 ord D-TKE, NL (Sun and Chang, 1986)	c: 2nd ord, 0.0003 s^{-1}	yes
COAMPSv3	Leapfrog 2nd ord	3	h+v: 2nd ord	1.5 ord MY-TKE, NL (Thompson and Burk, 1991)	c: 4th ord, 0.005 s^{-1}	no
COAMPSv4	Leapfrog 2nd ord	3	h+v: 2nd ord	1.5 ord MY-TKE, NL (Thompson and Burk, 1991)	c: 4th ord, 0.005 s^{-1}	no
EULAG	MPDATA 2nd ord	10	h+v: 2nd ord	1.5 ord D-TKE (Schumann, 1991)	TKE (isotropic)	yes
MM5	Leapfrog 2nd ord	3	h+v: 2nd ord	1st ord PBL, MF (Zhang and Anthes, 1982)	c: 4th ord, 0.001 s^{-1}	yes
RAMS	Leapfrog 2nd ord	5	h+v: 2nd ord	1.5 ord MY-TKE, NL (Helfand and Labraga, 1988)	Smagorinsky	yes
UM	SISL	10	SISL	1st ord PBL, NLD+MF (Lock et al., 2000)	none	no
WRF-TKE	Runge-Kutta 3rd ord	1	h: 5th ord v: 3rd ord	1.5 ord D-TKE	TKE (isotropic)	no
WRF-YSU	Runge-Kutta 3rd ord	1	h: 5th ord v: 3rd ord	1st ord PBL, NLD (Hong et al., 2006)	Smagorinsky v: none	no

3.2 Local boundary layer evolution

Figure 3 compares the boundary layer evolution in terms of profiles of potential temperature at 1200 LT at the four sites shown in Figure 1. A typical convective boundary layer (CBL) has developed over the plains, with mixed layer (ML) depths ranging from 300 m for RAMS to 1200 m for WRF-YSU. The ML is about 1-2 K cooler for ARPS than for the other models, and about 5 K cooler for RAMS. The cooler ML for ARPS and RAMS is due to the smaller surface sensible heat flux over the plains in those two models (see Figure 2). A well mixed CBL has also developed over the mountain ridge, with ML depths ranging from 600 m to 1000 m. A more complex temperature structure has developed at the two valley sites. The valley center site shows the typical three-layer structure found in many mountain valleys (Brehm, 1986; Weigel et al., 2006), with a well mixed layer near the ground separated by a stable layer from a second nearly neutral layer aloft. There are large differences in the simulated temperature structure between the models. The depth of the ML ranges from 200 m (RAMS) and 400 m (COAMPSv4) to 1300 m (WRF-YSU); the height of the lower boundary of the upper neutral layer varies between 1200 m (COAMPSv3) and 1700 m (WRF-YSU). The soundings over the valley slope exhibit a similar structure to the valley center site, but with a less marked stable layer, and somewhat less variation between the models.

3.3 Cross-valley circulation

Figure 4 depicts vertical profiles of the cross-valley wind speed over the western slope at $x = -6$ km at 0900, 1200, and 1500 LT. The differences between the models are relatively small in the morning, but quite large in the afternoon. The depth of the upslope wind layer growths from about 200 m at 0900 LT, to 300-500 m at 1200 LT, to over 500 m in some models in the afternoon. Note also the onset of the plain-to-basin wind about 500 m above ridge height, which is clearly visible in the 1200 LT sounding, and the large variability between the models in the simulated strength and structure of this wind, especially in the afternoon.

The time evolution of the upslope wind on the west slope at $x = -6$ km is shown in Figure 5. The wind starts soon after sunrise and increases in strength until noon/early afternoon. At 100 m above ground, the simulated evolution is initially quite similar, with the differences between the models increasing during the day. And in the afternoon, the models differ by more than two hours in the timing of the reversal to downslope flow. Closer to the ground surface, the differences between the models are much larger. The maximum upslope wind speed at 10 m above ground varies between less than 2 m s^{-1} for MM5 to more than 4 m s^{-1} for ARPS (RAMS has even larger wind speeds due to the open lateral boundary conditions).

3.4 Plain-to-basin circulation

The plain-to-basin circulation (east-west wind) is clearly visible in Figure 6, which depicts vertical profiles of the cross-ridge wind over the western ridge. By 1200 LT, there is a plain-to-basin flow in the lowest few hundred meters for all models except ARPS and RAMS, and a return basin-to-plain flow in a layer extending from about 500 m to 1200 m above ground. The retarded onset of the plain-to-basin circulation for the two models over the western ridge is likely due to the fact that they account for the dependence of solar radiation on the inclination of the surface. This leads to strong upslope flows on the east-facing slopes and a delayed evolution on the west-facing slopes. In contrast, the other models produce a symmetric evolution of the slope winds over east and west-facing slopes. While MM5 also takes the surface inclination into account, the near-surface wind is already from west to east at 1200 LT, due to the faster increase of the surface sensible heat flux in MM5 than in ARPS and RAMS (see Figure 2). By 1500, there is a plain-to-basin circulation in all models, but with large differences in its vertical structure.

3.5 Along-valley flow

Figure 7 shows vertical profiles of the along-valley wind at 1200 and 1500 LT over the valley center and the western slope. At 1200 LT there is good agreement in the simulation of the along valley wind between the models (except RAMS), the simulated maximum wind speed is about $5\,\mathrm{m\,s^{-1}}$. Some differences exist as to the depth of the along-valley wind layer which varies between 1200 m and 1500 m. At 1500 LT there are substantial differences in the vertical structure of the simulated along valley wind. The depth of the along-valley wind layer varies from 1000 m for COAMPSv4 to over 2000 m for WRF-YSU.

The time evolution of the along-valley wind for the valley center and the western slope is shown in Figure 8. Initially there is good agreement between the models which decreases rapidly, however, after noon. In the late afternoon, the simulated wind speeds vary by more than $3\,\mathrm{m\,s^{-1}}$. A similar decrease of agreement between the models is seen in Figure 9, which shows the along-valley variation of the along valley wind speed at 1200 and 1500 LT. As can be seen from Figure 10, which shows the along valley wind for the uncoupled simulations, identical forcing of the models through a prescribed surface sensible heat flux does not reduce the variability between the models. In contrast, the differences are even larger, likely due to the free-slip lower boundary condition used for the uncoupled simulations Note, however, that in terms of the mean, vertically-averaged, along valley wind the results for the uncoupled simulations are more similar than for the coupled simulations (not shown).

Figure 11 illustrates the similarities and differences in the spatial structure of the simulated along valley wind together with the cross-valley circluation. The figure is for 1200 LT, which is when the differences between the models are still relatively small. Nevertheless, the diversity of results is quite large. The depth of the along-valley flow layer in the valley center is quite shallow for the two COAMPS models, but it extends almost to the height of the mountain ridges for many of the other models. Also the along-valley flow has been advected by the cross-valley circulation above the mountain ridges for some models (COAMPSv3, UM), but not for others (ARPS, WRF-YSU).

4 CONCLUSIONS

We have presented a detailed intercomparison of six mesoscale models that are applied to simulate the evolution of the coupled boundary layer - valley wind system for an idealized valley-plain configuration. From the initial analysis of the results the following tentative conclusions can be drawn:

- There is good agreement between the models in their simulation of the initial development of the valley wind, between sunrise and noon. The agreement is particularly high in the lowest 500 m above ground level.
- The strength and spatial structure of the simulated along valley wind becomes more diverse after midday, as the along valley wind interacts with the cross-valley circulation and the turbulent boundary layers.
- While the initial temporal evolution and strength of the mean-along valley flow are primarily determined by the simulated surface energy balance — radiation, land surface, and atmospheric surface layer model —, the spatial structure and later development of the along-valley flow are strongly influenced by the mixing parameterizations (horizontal and vertical).
- There is less agreement between the models with respect to the simulated evolution of the local boundary layers. In the morning hours, the differences are primarily related to differences in the simulated surface energy balance and to differences in the intensity of vertical mixing induced by the PBL turbulence

schemes. In the afternoon hours, the differences between the models are also influenced by complex interactions between parameterized turbulence, computational mixing and the various thermally-induced mesoscale flows.

ACKNOWLEDGEMENTS

The first author was supported by the National Science Foundation's Physical and Dynamic Meteorology Division (S. Nelson, Program Manager) through grant ATM-0444205 and by the Swiss National Science Foundation (grant PA002-111427).

REFERENCES

Brehm, M., 1986: Experimentelle und numerische Untersuchungen der Hangwindschicht und ihrer Rolle bei der Erwärmung von Tälern. Ph.D. dissertation, Meteorologisches Institut, Universität München, 150 pp. [Wiss. Mitt. Nr. 54].

Grubisic, V., J. D. Doyle, J. Kuettner, S. Mobbs, R. B. Smith, C. D. Whiteman, R. Dirks, S. Czycyk, S. A. Cohn, S. Vosper, M. Weissmann, S. Haimov, S. De Wekker, L. Pan, and F. K. Chow, 2008: The Terrain-induced Rotor Experiment: An overview of the field campaign and some highlights of special observations. *Bull. Amer. Meteor. Soc.*, in press.

Helfand, H. M., and J. C. Labraga, 1988: Design of a nonsingular level 2.5 second-order closure model for the prediction of atmospheric turbulence. *J. Atmos. Sci.*, **45**, 113–132.

Hong, S.-Y., Y. Noh, and J. Dudhia, 2006: A new vertical diffusion package with an explicit treatment of entrainment processes. *Mon. Wea. Rev.*, **134**, 2318–2341.

Li, J. G., and B. W. Atkinson, 1999: Transition regimes in valley airflows. *Bound.-Layer Meteor.*, **91**, 385–411.

Lock, A. P., A. R. Brown, M. R. Bush, G. M. Martin, and R. N. B. Smith, 2000: A new boundary layer mixing scheme. Part I: Scheme description and single-column model tests. *Mon. Wea. Rev.*, **128**, 3187–3199.

Rampanelli, G., D. Zardi, and R. Rotunno, 2004: Mechanisms of up-valley winds. *J. Atmos. Sci.*, **61**, 3097–3111.

Schumann, U., 1991: Subgrid length-scales for large-eddy simulation of stratified turbulence. *Theoret. Comput. Fluid Dynamics*, **2**, 269–290.

Steinacker, R., 1984: Area-height distribution of a valley and its relation to the valley wind. *Contrib. Atmos. Phys.*, **57**, 64–71.

Sun, W.-Y., and C.-Z. Chang, 1986: Diffusion model for a convective layer. Part I: Numerical simulation of convective boundary layer. *J. Clim. Appl. Meteorol.*, **25**, 1445–1453.

Thompson, W. T., and S. D. Burk, 1991: An investigation of an Arctic front with a vertically nested mesoscale model. *Mon. Wea. Rev.*, **119**, 233–261.

Wagner, A., 1938: Theorie und Beobachtung der periodischen Gebirgswinde. *Gerl. Beitr. Geophys.*, **52**, 408–449.

Weigel, A. P., F. K. Chow, M. W. Rotach, R. L. Street, and M. Xue, 2006: High-resolution large-eddy simulations of flow in a steep Alpine valley. Part II: Flow structure and heat budgets. *J. Appl. Meteor. Climatol.*, **45**, 87–107.

Whiteman, C. D., 2000: *Mountain Meteorology: Fundamentals and Applications*. Oxford University Press, 355 pp.

Zhang, D., and R. A. Anthes, 1982: A high-resolution model of the planetary boundary layer — Sensitivity tests and comparison with SESAME-79 data. *J. Appl. Meteor.*, **21**, 1594–1609.

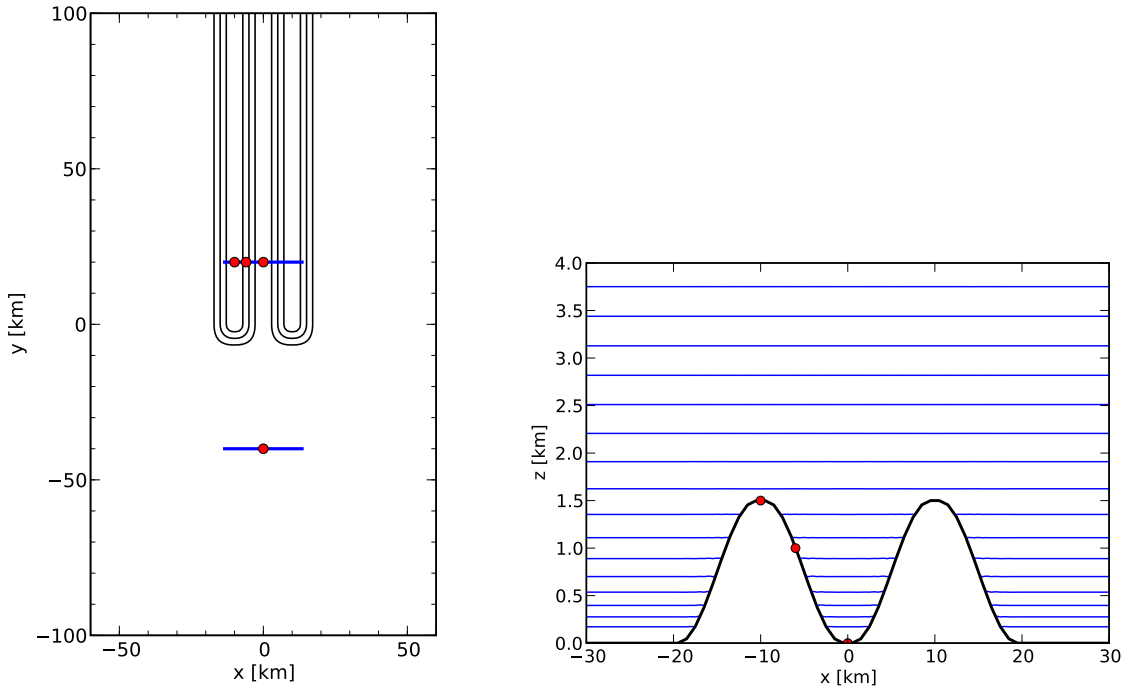

Figure 1: (a) Contour plot of the three-dimensional valley-plain topography (contour values are 250, 750, and 1250 m) and computational domain adopted; only the southern half of the domain is shown. The blue lines denote the location of the vertical cross sections and the red circles denote the location of the soundings to be shown. (b) Cross section of topography and initial potential temperature distribution.

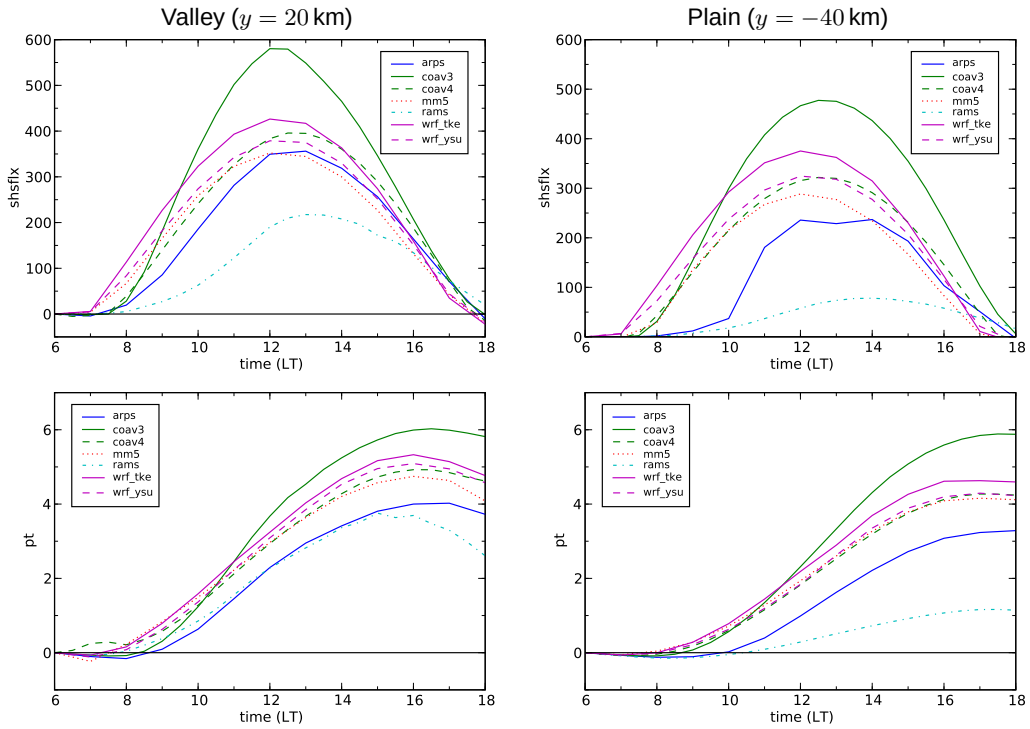

Figure 2: Time series of surface sensible heat flux (averaged from $x \pm 10$ km) and vertically-averaged potential temperature change at $x = 0$ km (average from the surface to 1500 m).

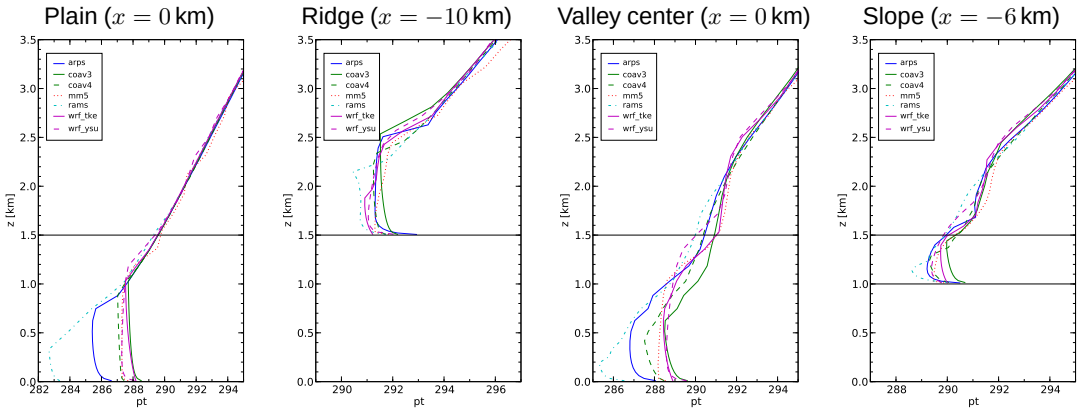

Figure 3: Profiles of potential temperature at 1200 LT at four different locations ($y = -40$ km for the plain, $y = 20$ km for the other three sites). The horizontal line indicates the height of the mountain ridge.

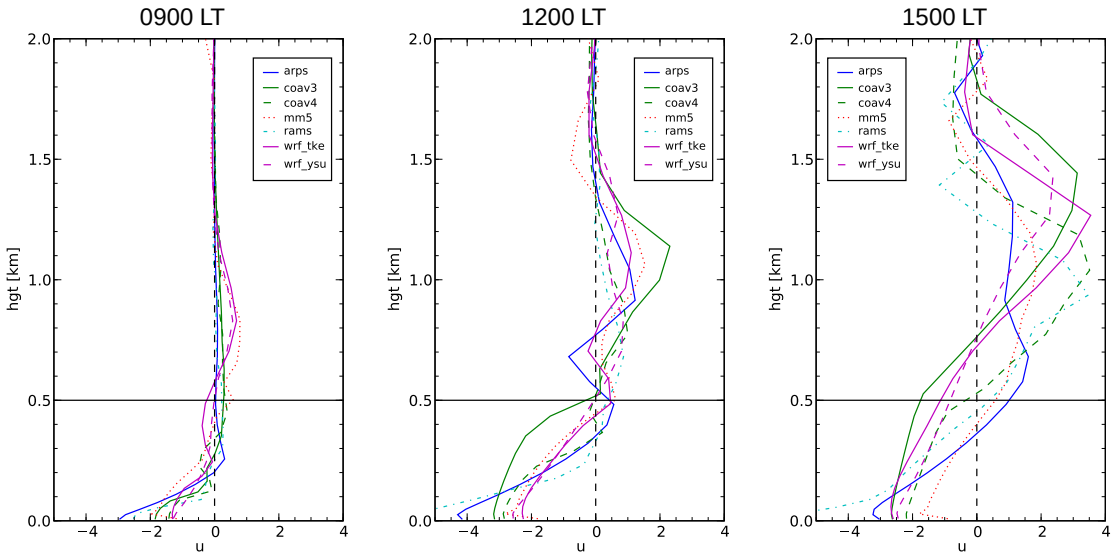

Figure 4: Profiles of cross-valley wind speed u over the western slope ($x = -6$ km, $y = 20$ km). The horizontal line indicates the height of the mountain ridge, and the y-axis denotes the height above ground level.

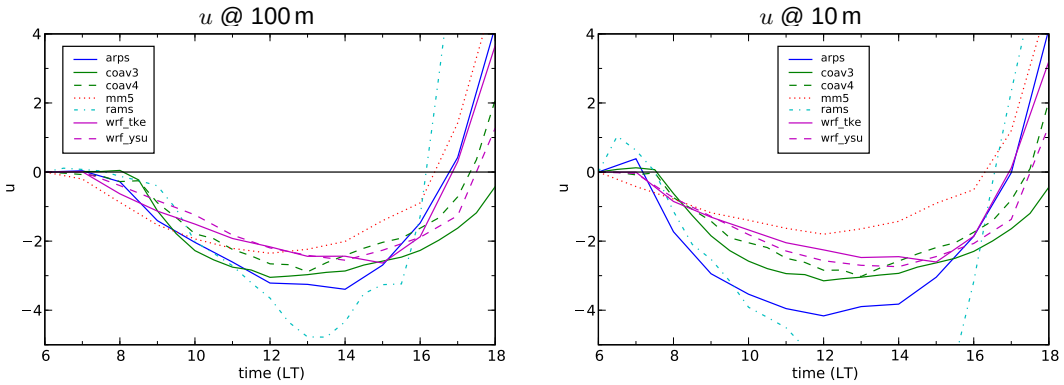

Figure 5: Time series of cross-valley wind speed u over the western slope ($x = -6$ km, $y = 20$ km).

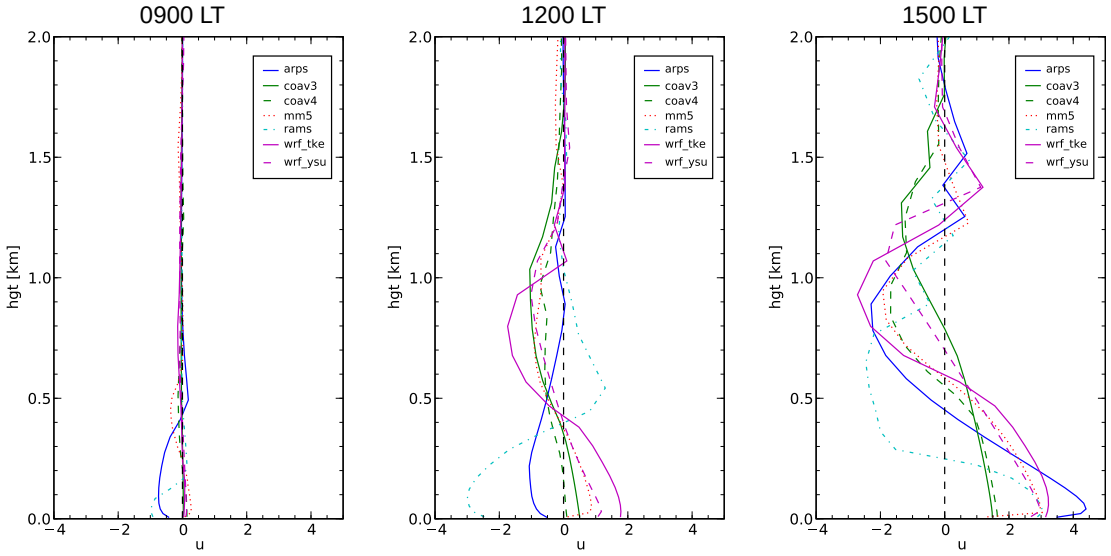

Figure 6: Profiles of cross-valley wind speed u over the western ridge ($x = -10$ km, $y = 20$ km).

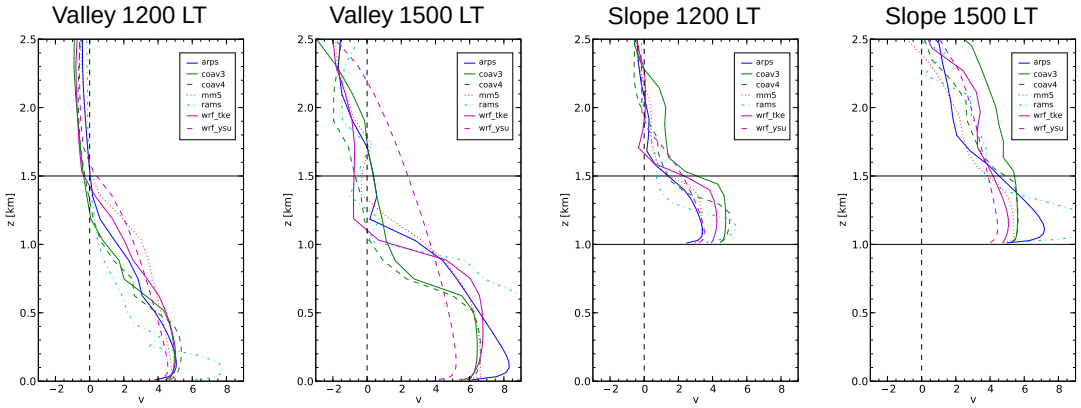

Figure 7: Profiles of along-valley wind at the valley center ($x = 0$ km) and over the western slope ($x = -6$ km). The along-valley position is $y = 20$ km.

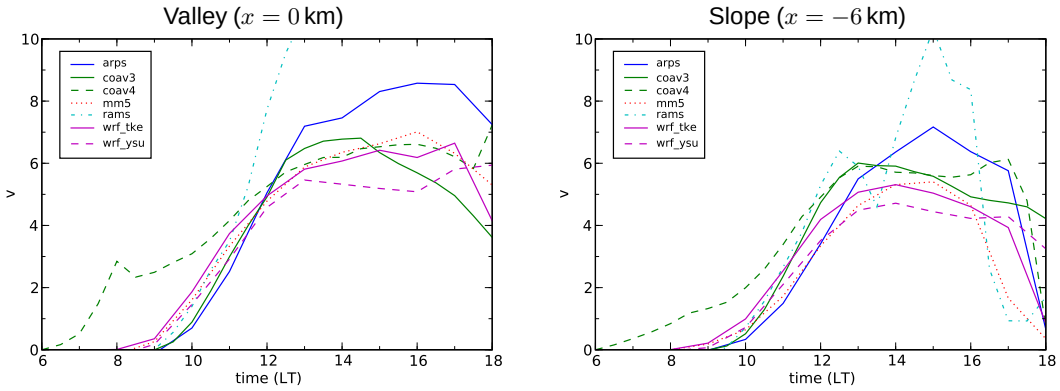

Figure 8: Time series of along-valley wind speed v at 100 m above ground level. The along-valley position is $y = 20$ km.

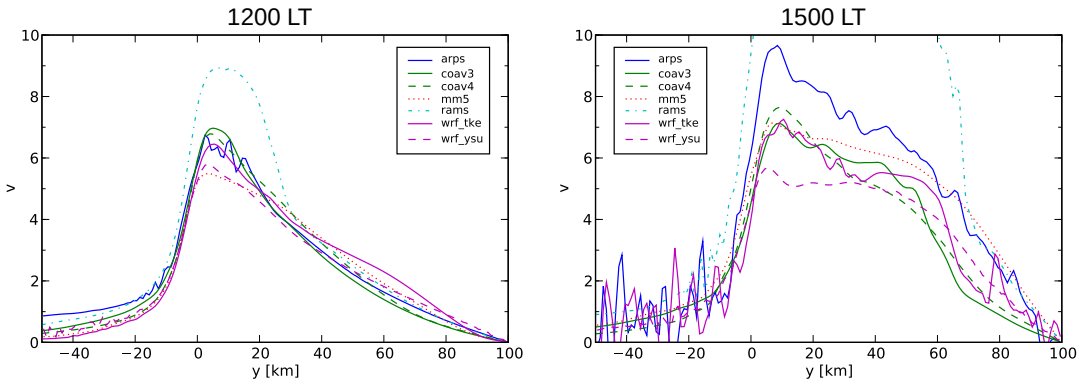

Figure 9: Along-valley variation of along-valley wind speed at 100 m above ground level.

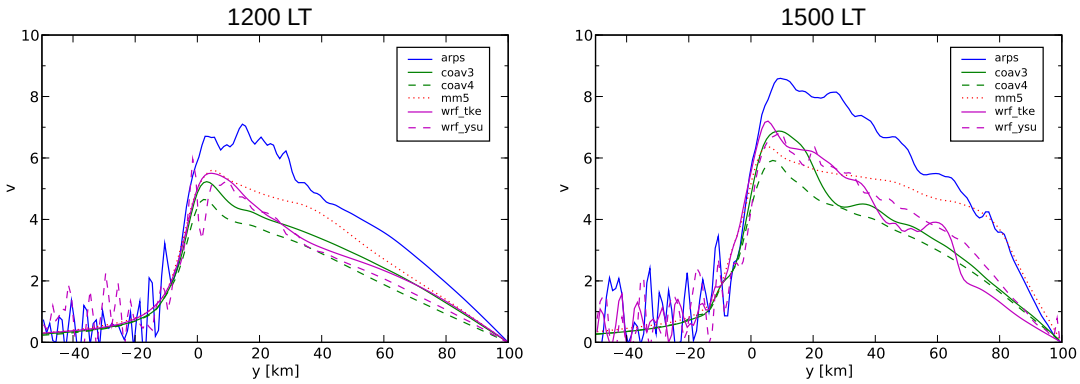

Figure 10: As in Figure 9, but for the uncoupled simulations.

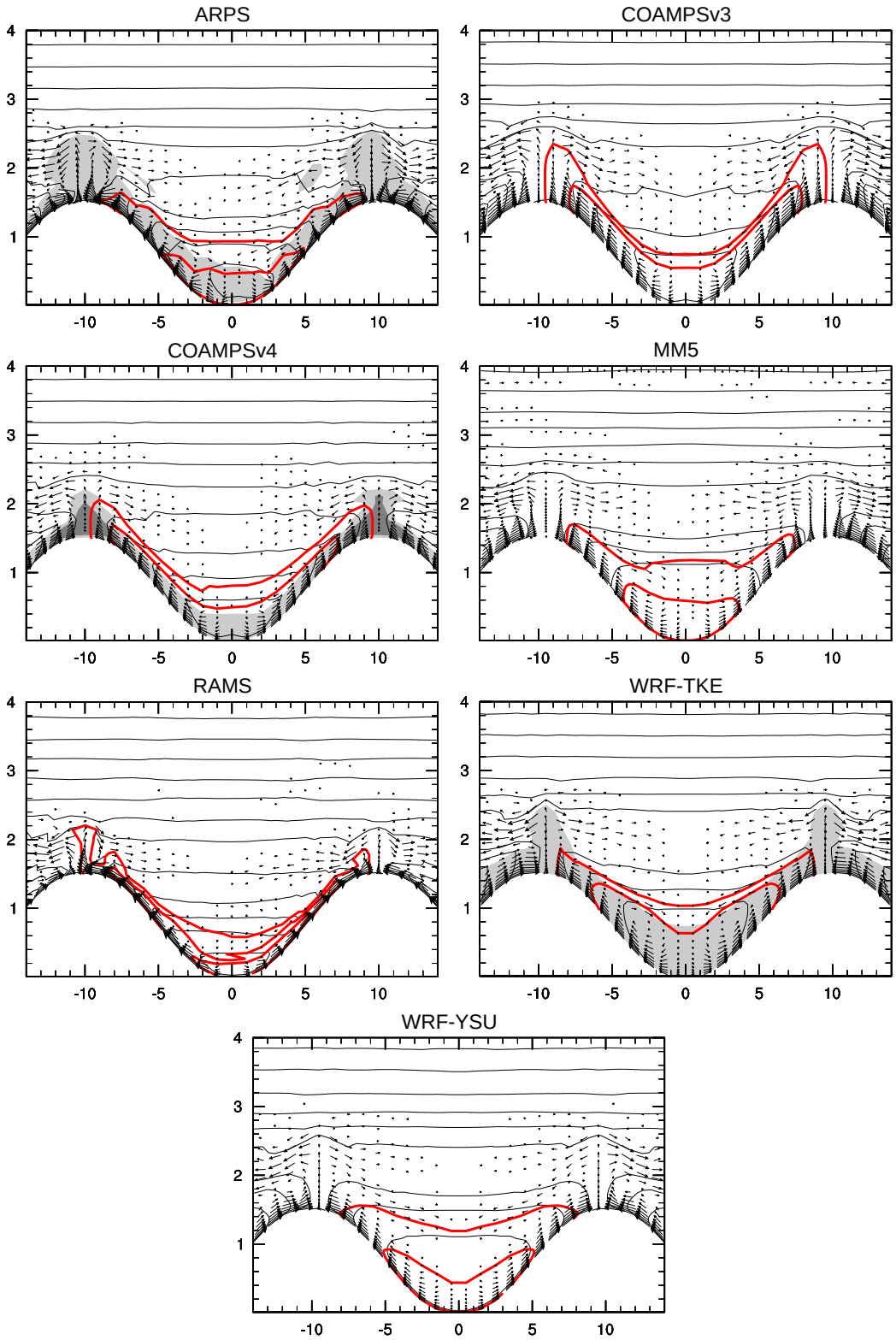

Figure 11: Snap-shot of the flow at 1200 LT in the west-east cross section at $y = 20$ km. Along-valley wind component (thick bold lines; contour interval 2 m s^{-1}), potential temperature (thin lines; contour interval 1 K), cross-valley circulation (vectors), and vertical diffusion coefficient (shading; 10 m^2 s^{-1}).